Three-Dimensional Developing Flow Model for Photocatalytic Monolith Reactors

Md. Moazzem Hossain and Gregory B. Raupp
Dept. of Chemical, Bio and Materials Engineering, Arizona State University, Tempe, AZ 85287

Steven O. Hay and Timothy N. Obee
United Technologies Research Center, East Hartford, CT 06108

A first-principles mathematical model describes performance of a titania-coated honeycomb monolith photocatalytic oxidation (PCO) reactor for air purification. The single-channel, 3-D convection–diffusion–reaction model assumes steady-state operation, negligible axial dispersion, and negligible homogeneous reaction. The reactor model accounts rigorously for entrance effects arising from the developing fluid-flow field and uses a previously developed first-principles radiation-field submodel for the UV flux profile down the monolith length. The model requires specification of an intrinsic photocatalytic reaction rate dependent on local UV light intensity and local reactant concentration, and uses reaction-rate expressions and kinetic parameters determined independently using a flat-plate reactor. Model predictions matched experimental pilot-scale formaldehyde conversion measurements for a range of inlet formaldehyde concentrations, air humidity levels, monolith lengths, and for various monolith/lamp-bank configurations. This agreement was realized without benefit of any adjustable photocatalytic reactor model parameters, radiation-field submodel parameters, or kinetic submodel parameters. The model tends to systematically overpredict toluene conversion data by about 33%, which falls within the accepted limits of experimental kinetic parameter accuracy. With further validation, the model could be used in PCO reactor design and to develop quantitative energy utilization metrics.

Introduction

Within enclosed living and working spaces, trace volatile organic contaminants (VOCs) are continually released by furnishings, equipment, and the occupants themselves. If these contaminants are allowed to concentrate in the indoor air, the resulting exposure to human occupants may cause eye and mucosal irritation, headaches, nausea, or allergic reactions. In addition to chemical contamination, microbiological contamination of indoor air can have potentially severe consequences. Once contaminated, a central air-handling system is a breeding ground for these microorganisms, effectively recirculating and distributing them throughout the building. Chronic illness caused by indoor air pollution, otherwise known as ''sick building syndrome,'' may be caused by either chemical or biological contamination, or in some cases may be caused by a synergistic interaction between VOCs and microorganisms (e.g., molds). In this context, the U.S. EPA has concluded that indoor air pollution poses a greater human health risk than outdoor air pollution (EPA Report, 1987).

Although elimination of the sources of contamination is the most desirable approach to controlling exposure, and thereby improving the health and safety of the building occupants, there are many instances where localized control is not possible, and other means of controlling indoor air quality are needed. Increasing the fresh-air intake rate to the building is the conventional approach to improving indoor air quality. This strategy provides a dilution effect, but does not completely eliminate the contaminants and associated human

Correspondence concerning this article should be addressed to G. B. Raupp.

exposure. Moreover, the increased fresh-air rate puts an additional energy load on the heating, ventilation, and air-conditioning (HVAC) system.

The ideal indoor-air-quality (IAQ) control technology would provide a high destruction rate for a variety of VOCs and for microbes, would be low cost and require little or no maintenance, could readily be installed or implemented in existing buildings, and would be inherently safe and environmentally benign. This latter constraint implies that the technology would not require use of hazardous or toxic chemicals. In addition, the basic technology would be viable as an integral part of an HVAC system, providing continuous active purification of the indoor air.

Gas–solid photocatalytic oxidation (PCO) (Dibble and Raupp, 1990, 1992; Raupp and Junio, 1993; Peral and Ollis, 1992; Fu et al., 1995; Luo and Ollis, 1996; Sauer et al., 1995; Obee, 1996; Nimlos et al., 1996; Hay et al., 1996) is an attractive candidate technology that may indeed meet these demanding requirements. This potential is derived from the following features of the photocatalytic process: (1) chemical activation is provided by ultraviolet (UV) light, allowing significant reaction rates at ambient temperatures; (2) apparent photon utilization can be quite high, offering the potential for an energy-efficient process; (3) the titania catalyst is inexpensive and is readily applied in a variety of physical forms; (4) the primary oxidant is derived from the air itself, precluding the need for addition of supplementary oxidants such as ozone or peroxide; and (5) complete oxidation to relatively innocuous products is possible. Moreover, recent evidence suggests that the PCO process is capable of killing a variety of airborne pathogenic microorganisms (Hay et al., 1996; Kikuchi et al., 1997; Sunada et al., 1998).

Perhaps the most significant unresolved technical barrier to successful widespread commercialization is optimum photocatalytic reactor configuration and design (National Research Council, 1991). It is relatively straightforward to design a laboratory-scale reactor that simultaneously contacts a uniformly irradiated catalyst and air effectively. At the commercial level, however, design of a physically compact photocatalytic reactor that simultaneously and efficiently contacts the activating light, solid catalyst, and the contaminated gas while providing high photon utilization is not straightforward. For integration of PCO for air purification in HVAC systems in office buildings and factories, it is crucial that the design be characterized by relatively low power consumption. This requirement implies that the PCO unit must yield low-pressure drop operation and must utilize the UV photons efficiently.

Honeycomb monolith reactors provide nearly negligible pressure drop and are widely used in automobile exhaust emission control and for NO_x reduction in power-plant flue gases. Figure 1 shows the reactor configuration envisioned for PCO-based air purification. Successive alternating banks of UV lamps and honeycomb monoliths are mounted directly in the HVAC duct. The UV lamps are low-pressure mercury ''black'' lamps emitting in the 300–400-nm range, with peak emission at 365 nm, or are germicidal lamps emitting primarily at 254 nm. The lamps irradiate the monolith front and back faces. Air flowing in the duct is forced through the monolith channels, which are coated with the active titania photocatalyst.

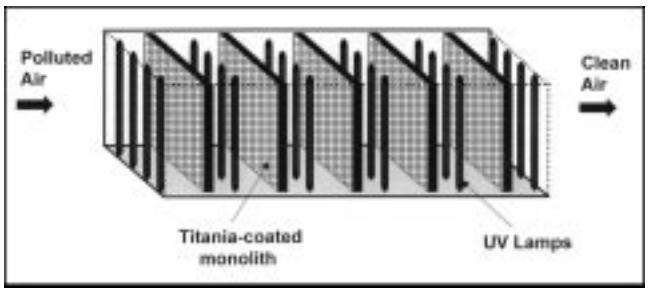

Figure 1. Full-scale photocatalytic honeycomb monolith reactor.

Reactor performance is determined by the UV radiation profile in the channel and the interaction of convection, diffusion, and reaction of the contaminant. In the absence of a valid photocatalytic reactor model, the PCO unit must be designed through an empirical, trial-and-error process that neither guarantees an energy-efficient design, nor provides an understanding of the practical capabilities and limits of the technology. The purpose of this article is to provide a sound theoretical basis for quantifying the inherent UV energy utilization and indoor air purification capabilities and limitations of the honeycomb monolith configuration.

The literature contains extensive work on *thermal* catalytic monolith reactor modeling (Young and Finlayson, 1976; Vortuba et al., 1975a,b; Hayes et al., 1992, 1996; Groppi et al., 1995a,b). These modeling efforts have focused on the analysis of strong thermal effects, multiplicity of steady states, and other phenomena associated with rapid exothermic reactions. These models have little direct relevance for PCO, since thermal-energy contributions to the energy-conservation statement are negligible in general; instead energy conservation is dominated by UV radiation accounting.

Analyses of monolith reactors addressing the issues specific to PCO applications are scarce in the scientific literature. Luo (1994) developed a model for a photocatalytic oxidation monolith reactor in which square channels were approximated as circular. Two simple UV light distributions were employed to bracket the range of expected performance under conditions of developing flow: (1) uniform light intensity, and (2) a $1/r^2$ profile where r is the distance from a point light source. Nicolella and Rovatti (1998) developed a plug-flow model for a monolith channel irradiated by an external focused source that combined photocatalytic and thermal reactions to identify operating regimes controlled by photonic and thermal effects. The ultraviolet intensity distribution was estimated with a geometric monochromatic submodel that assumed negligible reflection by the catalyst. Because of the overly simplistic or inaccurate radiation-field submodels employed, neither the Luo nor the Nicolella and Rovatti models are sufficiently accurate to be employed as a simulator for reactor design purposes.

At ASU we recently developed and validated a first-principles radiation-field model for both circular-channel and square-channel monoliths coated with a *reflecting* photocatalyst layer (Hossain and Raupp, 1998a, 1999). This model was employed for circular channels in the limits of plug flow and fully developed laminar flow to identify limiting process performance behavior in terms of controlling dimensionless

groups (Hossain and Raupp, 1998b). It is important to note that our rigorous radiation-field model predictions reveal that the UV light intensity dies away at a distance into the monolith channel that is comparable to the laminar-flow entrance length (Hossain and Raupp, 1998a, 1999). As a consequence, the assumption of plug flow or fully developed laminar flow precludes accurate prediction of the enhanced mass transfer expected in the entrance length or developing flow region of the monolith.

Hall and coworkers at UTRC (Hall et al., 1996; Bendfeldt et al., 1997, 1998) developed a one-dimensional model for a single monolith channel that incorporates gas–solid mass-transfer coefficients for square monoliths averaged over the channel length. The model employs a monochromatic radiation field model that approximates the square channels as circular tubes, but rigorously accounts for diffuse reflectance of the thin catalyst film coated on the channel walls. Based on our comparisons of circular-channel and square-channel radiation-field-model predictions, the circular-channel approximation does not introduce significant inaccuracy in the model for low film reflectivities (Hossain and Raupp, 1998a). The UTRC model predictions are in good agreement with experimental conversion measurements for formaldehyde, toluene, and ammonia in a pilot-scale monolith-based air-purification unit (Bendfeldt et al., 1997, 1998).

In the present article we develop an integrated first-principles, mathematical model for simultaneous convection, diffusion, and reaction in a square-channel monolith reactor that incorporates the previously developed radiation-field submodel to describe the photocatalytic oxidation of dilute contaminants in air. Model assumptions are largely consistent with those employed in the prior model of Hall at UTRC (Hall et al., 1996). However, because the model employs a rigorous description of the three-dimensional developing flow field and concentration field, local mass-transfer rates are determined by local diffusive fluxes and local convective fluxes rather than by average mass-transfer coefficients.

Model Development

The monolith is composed of a large number of parallel channels whose conditions are presumed to be identical when assuming uniform distribution of variables at the monolith inlet. Under this hypothesis the simulation of the entire multichanneled monolith reduces to the analysis of a single channel. For a monolith experiencing significant gradients across its face, this single-channel model could be used to simulate each channel independently.

The single-channel monolith model incorporates a rigorous three-dimensional representation of the developing flow field and simultaneous gas-phase diffusion and heterogeneous reaction. This convection–diffusion–reaction model relies on our previously developed first-principles radiation-field submodel, and employs independently determined photocatalytic reaction-rate expressions and kinetic parameters.

UV radiation-field submodel

In this section we briefly describe our recently developed and validated radiation-field model for a channeled monolith photocatalytic reactor (Hossain and Raupp, 1998a, 1999). The model accounts for photon transport, absorption, and reflection in a square-monolith channel with geometry as defined in Figure 2a. The principal assumptions of the model are as follows:

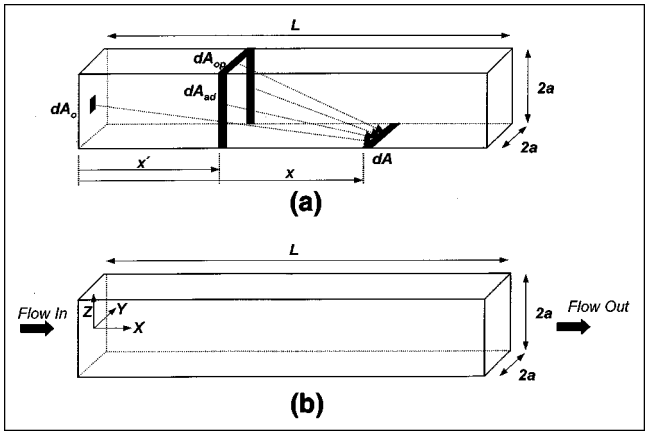

Figure 2. Monolith channel of square cross section showing (a) the differential areas contributing photon flux to a differential wall-strip element *dA*, and (b) the coordinate system for the convection–diffusion–reaction model.

1. All channels of the monolith are identically irradiated externally at their respective channel entrances by a lamp or lamps that can be approximated by a time-invariant, diffuse polychromatic light source.
2. Gas-phase absorption, scattering, and reflection of the light is negligible.
3. The photocatalytic thin-film coating on the monolith walls is uniform and sufficiently thick such that no light transmits through the thin film.
4. Light reflection from the thin-film coating is perfectly diffuse.
5. Optical thin-film properties (absorbance and reflectance) are light-wavelength dependent.
6. Optical thin-film properties (absorbance and reflectance) are independent of light incidence angle.
7. The thin film does not emit radiation in the spectral region of interest.

In the UTRC pilot-scale monolith reactor, the parallel lamp banks yield an ultraviolet light-intensity range of $\pm 10\%$ about the mean value employed in the simulations (Bendfeldt et al., 1997). The variation is periodic and reflects the parallel-bank arrangement of the UV lamps. Although one could relax assumption (1) and model a set of channels with different incident UV intensities, the modest level of variation and periodic nature of the variation both suggest that use of a mean UV irradiation intensity should yield reasonably accurate simulations.

Figure 2a shows the contributions of UV radiation incident on a differential wall area dA. Light strikes dA directly from the source dA_o and after reflection from the opposite wall dA_{op} and the two adjacent walls dA_{ad}. The mathematical representation of this model takes the form of the following integral equation for the dimensionless UV light-intensity

profile down the length of the channel (Hossain and Raupp, 1999):

$$\Phi_w(\lambda) = F\{dA;\, A_o\} + 2\cdot\rho(\lambda)\int_{A'_{ad}} \Phi_w(\lambda)\, dF\{dA;\, dA'_{ad}\} + \rho(\lambda)\int_{A'_{op}} \Phi_w(\lambda)\, dF\{dA;\, dA'_{op}\} \quad (1)$$

$$\Phi_{average} = \frac{\int_{\lambda_{min}}^{\lambda_{max}} P(\lambda)\cdot\Phi(\lambda)\, d\lambda}{\int_{\lambda_{min}}^{\lambda_{max}} P(\lambda)\, d\lambda}, \quad (2)$$

where Φ_w is the dimensionless UV flux to the channel wall; $\Phi_{average}$ is the integral average UV flux to the channel wall; ρ is the titania-coated wall reflectivity; and F and dF are geometrically determined integral and differential view factors, respectively, for the areas previously defined. The necessary dimensionless view factors (Siegel and Howell, 1992; Worth et al., 1996) have been previously derived and are given below in terms of dimensionless axial distance defined as $X \equiv x/2a$:

$$F\{dA;\, A_o\} = \frac{1}{\pi}\left[\tan^{-1}\frac{1}{X} + \frac{X}{2}\ln\frac{X^2(X+2)}{(X^2+1)^2} - \frac{X}{(X^2+1)^{1/2}}\tan^{-1}\frac{1}{(X^2+1)^{1/2}}\right] \quad (3)$$

$$dF\{dA;\, dA'_{op}\} = \frac{1}{\pi}\left(|X-X'|^2+1\right)^{-3/2} \times \tan^{-1}\frac{1}{\left(|X-X'|^2+1\right)^{1/2}}\, dX' \quad (4)$$

$$dF\{dA;\, dA'_{ad}\} = -\frac{1}{4\pi}\ln\frac{|X-X'|^2\left(|X-X'|^2+2\right)}{\left(|X-X'|^2+1\right)^2}\, dX'. \quad (5)$$

Substitution of these view factors into Eq. 1 yields an integral expression for the axial flux distribution to the channel wall, where the integration limits on X' are from 0 to α.

The VOC conversion experiments described below employ germicidal lamps that emit primarily (98%) at 254 nm. For purposes of model validation, a monochromatic source at 254 nm was assumed. Film reflectivity at 254 nm was estimated from the following empirical reflectivity expression (Brucato et al., 1997; Hossain and Raupp, 1999):

$$\rho(\lambda) = 0.515 + 0.455\cdot\tanh\left[\left(\frac{\lambda-420}{20}\right)+1.85\right]. \quad (6)$$

The model equations are solved numerically to determine the UV flux profile, which is an input to our convection–diffusion–reaction model.

Velocity field

Most of the monolith modeling work in the literature neglects the fluid-flow entrance effect. Instead, it is usually assumed that the velocity field is fully developed laminar flow or plug flow throughout the monolith, and that the concentration field is also fully developed. Although these simplifying assumptions considerably reduce the calculation effort, they likely lead to considerable model inaccuracy in PCO modeling, as explained in the following text. For a square duct, the criterion for the entrance length in which the velocity profile will be fully developed is $x_{FD}/d_H = 0.09\cdot Re$, where Re is the Reynolds number, x_{FD} is the entrance length, and d_H is the hydraulic diameter (Goldstein and Kreid, 1967). For photocatalytic monolith air purifiers in HVAC systems, convective transport will be confined to the laminar flow region. Our validated radiation-field model prediction shows that a monolith irradiated from one side is essentially dark after five-channel-diameter lengths. Since light intensities are additive, for the case of irradiation from both sides, the effective irradiated length would be around ten channel-diameters. If we assume that the length of the reactor is equal to the effective irradiated length, for a Reynolds number of 100, the entrance length would be 90% of the entire monolith reactor length. More importantly, most of the conversion will take place at the reactor entrance where the light intensity is highest. It is therefore clear that to ensure accurate model predictions we need to consider the developing fluid flow field.

In this article we therefore develop a rigorous first-principles model for a square cross-section channeled monolith photocatalytic reactor that accounts for three-dimensional, developing fluid flow, diffusion, and simultaneous heterogeneous reaction. The mathematical representation of the model takes the form of the governing mass and momentum conversion statements and species mass accounting statements. At high Reynolds number ($Re \gg 1$), the axial diffusion term in the three momentum equations can be neglected (Howang et al., 1993). The axial dispersion of mass in the fluid may be neglected for Peclet numbers ($Pe_m = ReSc$) greater than 50 (Young and Finlayson, 1976). For a typical VOC, Sc is on the order of unity, so, for a Re of 50 or higher the axial dispersion can be neglected. For expected commercial monolith dimensions and HVAC air flow rates, values for Re exceed 100. For the simulations presented in this article, Re values range from 57 to 412. We therefore assume negligible axial dispersion of mass and momentum.

Additional model assumptions are summarized as follows:

1. Steady-state conditions
2. Isothermal conditions along the monolith channel
3. Uniform air velocity before the channel entrance
4. Dilute solution (dilute contaminants in air)
5. Incompressible Newtonian fluid with constant physical properties
6. Heterogeneous reaction takes place only at the reactor wall; homogeneous reactions are negligible.

The uniform velocity assumption (assumption 3) implies that there is no flow development or velocity profile disturbance upstream of the channel entrance. This assumption is a direct consequence of the negligible axial diffusion assumption, since in this limit a more rigorous model account-

ing for upstream entrance effects reduces to the model presented here (Vrentas et al., 1966). Simulations for flow in cylindrical channels show that there is negligible upstream velocity field disturbance for $Re \geq 150$ (Vrentas et al., 1966). We therefore expect that the model presented here provides a good representation of the physical reality for Reynolds numbers greater than about 150 (which includes the large majority of the simulations presented in this article), but introduces some inaccuracy in the developing flow field for Re numbers between 50 and 150.

Under these assumptions the governing equations for the velocity field become

$$\rho\left(v_x\frac{\partial v_x}{\partial x}+v_y\frac{\partial v_x}{\partial y}+v_z\frac{\partial v_x}{\partial z}\right) = -\frac{\partial p}{\partial x}+\mu\left(\frac{\partial^2 v_x}{\partial y^2}+\frac{\partial^2 v_x}{\partial z^2}\right) \quad (7)$$

$$\rho\left(v_x\frac{\partial v_y}{\partial x}+v_y\frac{\partial v_y}{\partial y}+v_z\frac{\partial v_y}{\partial z}\right) = -\frac{\partial p}{\partial y}+\mu\left(\frac{\partial^2 v_y}{\partial y^2}+\frac{\partial^2 v_y}{\partial z^2}\right) \quad (8)$$

$$\rho\left(v_x\frac{\partial v_z}{\partial x}+v_y\frac{\partial v_z}{\partial y}+v_z\frac{\partial v_z}{\partial z}\right) = -\frac{\partial p}{\partial z}+\mu\left(\frac{\partial^2 v_z}{\partial y^2}+\frac{\partial^2 v_z}{\partial z^2}\right) \quad (9)$$

$$\frac{\partial v_x}{\partial x}+\frac{\partial v_y}{\partial y}+\frac{\partial v_z}{\partial z}=0. \quad (10)$$

Here, the axial coordinate is x, and the transverse coordinates are y and z. The origin of the coordinate system is at the center of the channel inlet as shown in Figure 2b. The boundary conditions are uniform axial velocity u_o and pressure p_o at the duct entrance, zero normal and tangential velocities at the duct walls, and symmetry at the channel center line. The symmetry condition at the cross-section center line permits the restriction of the solution to one quadrant of the duct, as suggested in Figure 2b.

By using the concept of pressure deviation (Hwang et al., 1993), the pressure can be written as

$$p(x,y,z)=p_o+\bar{p}(x)+p'(x,y,z), \quad (11)$$

where p_o is the uniform inlet pressure, $\bar{p}(x)$ is the additional pressure averaged over the cross section at axial location x, and $p'(x,y,z)$ is the pressure deviation in the transverse direction. An order-of-magnitude analysis (Chou and Hwang, 1987) reveals that the axial pressure gradient $\partial p/\partial x$ is a function of x only since $d\bar{p}/dx \gg \partial p'/\partial x$. The term $\partial p'/\partial x$ is then eliminated in the axial momentum equation (Eq. 7).

Referring to the coordinate system in Figure 2b, the following dimensionless variables can be introduced for position, velocity, and pressure, respectively:

$$X=\frac{x}{2a},\quad Y=\frac{y}{2a},\quad Z=\frac{z}{2a},\quad X^+=\frac{X}{Re},$$
$$U=\frac{v_x}{u_o},\quad V=\frac{v_y Re}{u_o},\quad W=\frac{v_z Re}{u_o},$$
$$P=\frac{\bar{p}}{\rho u_o^2},\quad P'=\frac{p' Re^2}{\rho u_o^2},\quad Re=\frac{2a\rho u_0}{\mu}. \quad (12)$$

Then the dimensionless governing equations for velocity field become

$$U\frac{\partial U}{\partial X^+}+V\frac{\partial U}{\partial Y}+W\frac{\partial U}{\partial Z}=-\frac{dP}{dX^+}+\left(\frac{\partial^2 U}{\partial Y^2}+\frac{\partial^2 U}{\partial Z^2}\right) \quad (13)$$

$$U\frac{\partial V}{\partial X^+}+V\frac{\partial V}{\partial Y}+W\frac{\partial V}{\partial Z}=-\frac{\partial P'}{\partial Y}+\left(\frac{\partial^2 V}{\partial Y^2}+\frac{\partial^2 V}{\partial Z^2}\right) \quad (14)$$

$$U\frac{\partial W}{\partial X^+}+V\frac{\partial W}{\partial Y}+W\frac{\partial W}{\partial Z}=-\frac{\partial P'}{\partial Z}+\left(\frac{\partial^2 W}{\partial Y^2}+\frac{\partial^2 W}{\partial Z^2}\right) \quad (15)$$

$$\frac{\partial U}{\partial X^+}+\frac{\partial V}{\partial Y}+\frac{\partial W}{\partial Z}=0. \quad (16)$$

The boundary conditions, written in dimensionless form, are

At the inlet

$$X^+=0: \qquad U-1=V=W=P=0. \quad (17)$$

At the walls

$$(Y=0.5): \qquad U=V=W=0 \quad (18)$$

$$(Z=0.5): \qquad U=V=W=0. \quad (19)$$

At the cross-section centerplanes

$$Y=0: \qquad V=\frac{\partial U}{\partial Y}=\frac{\partial W}{\partial Y}=\frac{\partial P'}{\partial Y}=0 \quad (20)$$

$$Z=0: \qquad \frac{\partial U}{\partial Z}=\frac{\partial V}{\partial Z}=\frac{\partial P'}{\partial Z}=W=0. \quad (21)$$

A vorticity-velocity method developed by Chou and Hwang (1987) is employed to solve these equations. A vorticity function in the axial direction is defined as:

$$\xi=\frac{\partial W}{\partial Y}-\frac{\partial V}{\partial Z}. \quad (22)$$

By differentiating Eq. 22 with respect to Z and Y, respectively, and combining the result with the continuity equation (Eq. 16), the following equations can be derived:

$$\frac{\partial^2 V}{\partial Y^2}+\frac{\partial^2 V}{\partial Z^2}=-\frac{\partial \xi}{\partial Z}-\frac{\partial^2 U}{\partial Y \partial X^+} \quad (23)$$

$$\frac{\partial^2 W}{\partial Y^2}+\frac{\partial^2 W}{\partial Z^2}=\frac{\partial \xi}{\partial Y}-\frac{\partial^2 U}{\partial Z \partial X^+}. \quad (24)$$

The pressure terms in Eqs. 14 and 15 are eliminated by differentiating Eq. 14 with respect to Z and Eq. 15 with respect to Y, and subtracting the resulting equations from each other. We then employ the definition of vorticity (Eq. 22) to obtain the following equation for axial vorticity:

$$U\frac{\partial \xi}{\partial X^+} + V\frac{\partial \xi}{\partial Y} + W\frac{\partial \xi}{\partial Z} + \xi\frac{\partial V}{\partial Y} + \xi\frac{\partial W}{\partial Z} + \frac{\partial U}{\partial Y}\frac{\partial W}{\partial X^+} - \frac{\partial U}{\partial Z}\frac{\partial V}{\partial X^+} = \frac{\partial^2 \xi}{\partial Y^2} + \frac{\partial^2 \xi}{\partial Z^2}. \quad (25)$$

Equations 13, 23, 24, and 25 are used for solving for U, V, W, and ξ, respectively. An additional constraint to determine dP/dX^+ in Eq. 13 is derived from an overall mass balance. This balance can be expressed as

$$4\int_0^{0.5}\int_0^{0.5} U\,dY\,dZ = 1.0. \quad (26)$$

Concentration field

The mass-balance equation for the ith species can be written as

$$v_x\frac{\partial c_i}{\partial x} + v_y\frac{\partial c_i}{\partial y} + v_z\frac{\partial c_i}{\partial z} = D_i\left(\frac{\partial^2 c_i}{\partial y^2} + \frac{\partial^2 c_i}{\partial z^2}\right), \quad (27)$$

where c_i is the local concentration of species i and D_i is the diffusivity of i in air. By defining the dimensionless concentration as $C_i = c_i/c_{io}$, and using the other dimensionless variable previously defined, the governing equation for concentration field becomes

$$U\frac{\partial C_i}{\partial X^+} + V\frac{\partial C_i}{\partial Y} + W\frac{\partial C_i}{\partial Z} = \frac{1}{Sc}\left(\frac{\partial^2 C_i}{\partial Y^2} + \frac{\partial^2 C_i}{\partial Z^2}\right). \quad (28)$$

The boundary conditions, written in dimensionless form, are:

At the inlet

$$X^+ = 0: \qquad C_i = 1. \quad (29)$$

At the cross-section centerplanes

$$(Y = 0): \qquad \frac{\partial C_i}{\partial Y} = 0 \quad (30)$$

$$(Z = 0): \qquad \frac{\partial C_i}{\partial Z} = 0. \quad (31)$$

At the channel walls

$$(Y = 0.5): \qquad \frac{\partial C_i}{\partial Y} = -\left(\frac{2a}{D_i c_{io}}\right)\Re_i \quad (32)$$

$$(Z = 0.5): \qquad \frac{\partial C_i}{\partial Z} = -\left(\frac{2a}{D_i c_{io}}\right)\Re_i, \quad (33)$$

where $\Re_i$ is the local areal heterogeneous reaction rate. To complete the model, a reaction-rate expression valid over the entire range of local conditions (reactant and product concentrations, UV flux) is needed. We use the following semiempirical Langmuir-Hinshelwood-Hougen-Watson (LHHW) kinetic-rate form for the rate of reaction per unit surface area suggested by Obee (1996):

$$\Re(C_{\mathrm{VOC}}, C_W, I_G) = K_o\left\{\frac{K_1 C_{\mathrm{VOC}}}{1 + K_1 C_{\mathrm{VOC}} + K_2 C_W}\right\}\left\{\frac{K_4 C_W}{1 + K_3 C_{\mathrm{VOC}} + K_4 C_W}\right\} \quad (34)$$

where K_o (μ·mol/cm^2·h) is the reaction-rate constant for a given UV intensity (I_G); K_1, K_2, K_3, K_4 (ppm$_v^{-1}$) are the Langmuir adsorption equilibrium constants; and C_{VOC} (ppm$_v$) and C_W (ppm$_v$) are the gas-phase concentrations of the contaminant and water vapor, respectively. This model implies that two sites are involved in the rate-determining step for photocatalytic destruction, and that the VOC and water vapor compete for sites on the catalyst surface. The rate parameters for formaldehyde and toluene are taken from Obee (1996), and are based on one-factor-at-a-time kinetic experiments employing a continuous, slit flow, glass-plate photoreactor.

Upon substitution of this rate expression, the wall boundary conditions become

$$(Y = 0.5): \qquad \frac{\partial C_i}{\partial Y} = -\left(\frac{2a}{D_i c_{io}}\right)\left(\frac{I}{I_G}\right)^n \Re(C_{\mathrm{VOC}}, C_W, I_G) \quad (35)$$

$$(Z = 0.5): \qquad \frac{\partial C_i}{\partial Z} = -\left(\frac{2a}{D_i c_{io}}\right)\left(\frac{I}{I_G}\right)^n \Re(C_{\mathrm{VOC}}, C_W, I_G), \quad (36)$$

where I (mW/cm^2) is the UV flux incident on the monolith wall, and I_G (mW/cm^2) is the UV flux to the glass-plate reactor for which the kinetic constant has been evaluated. The exponent n for dilute formaldehyde and toluene in air was found to be 0.55 (Obee and Brown, 1995) for both compounds. For a conservative estimate we use the limiting value of 0.50 in our simulations.

After the velocity and concentration fields along the transverse directions are obtained, the mixing cup average concentrations at all axial locations are computed, as defined by

$$\overline{C}_i = \frac{\int_0^{0.5}\int_0^{0.5} UC_i\,dY\,dZ}{\int_0^{0.5}\int_0^{0.5} U\,dY\,dZ}. \quad (37)$$

Calculation of fractional conversion of the contaminant (reactant) is then straightforward.

Numerical Solution

The model equations (Eqs. 13, 23, 24, 25, and 28) constitute a system of nonlinear partial differential equations (PDEs) with complex nonlinear boundary conditions. A numerical finite difference scheme based on the vorticity–velocity method developed by Chou and Hwang (1987) is employed to obtain the simultaneous solution for the unknowns U, V, W, ξ, and C at each desired axial location as follows:

1. Assign initial values for the velocity components, vorticity, and concentration, at the inlet, $X^+ = 0$: $U - 1 = V = W = \xi = C - 1 = 0$.

2. Using a guessed value of the average axial pressure gradient, find new U and ξ values at interior points of the next axial position from Eqs. 13 and 25, respectively, by the DuFort-Frankel method (Roache, 1971).

3. Check if the constraint for the axial velocity in Eq. 26 is satisfied. If not, adjust the value of the pressure gradient in Eq. 13, and repeat steps 2 and 3.

4. Solve the elliptic-type equations (Eqs. 23 and 24) for V and W using a Gauss-Seidel iteration method (Carnahan et al., 1969). During the iteration process, values of vorticity ξ on the boundaries are evaluated (Chou and Hwang, 1987) simultaneously with V and W at the interior points.

5. Repeat step 4 until the following error criteria are satisfied for velocity components V and W:

$$\epsilon_1 = \frac{\sum \left| \left(V_{j,k}^{(n+1)} - V_{j,k}^{n} \right) / V_{j,k}^{(n+1)} \right|}{M \cdot N} \leq 10^{-4} \qquad (38)$$

$$\epsilon_2 = \frac{\sum \left| \left(W_{j,k}^{(n+1)} - W_{j,k}^{n} \right) / W_{j,k}^{(n+1)} \right|}{M \cdot N} \leq 10^{-4}, \qquad (39)$$

where M and N are the number of grid points in the Y and Z directions.

6. Obtain new values of concentration at interior points of the next axial location from Eq. 28 by the DuFort-Frankel method. Using the boundary conditions in Eqs. 35 and 36, iteratively compute the concentration at the channel walls through successive substitution.

7. Calculate the mixing-cup average concentration using Eq. 37.

8. Repeat steps 2 to 7 at the next axial position until the desired axial location is reached.

A uniform cross-sectional grid of 21×21 with fixed axial step size of 2.5×10^{-5} was used for the full domain of the square duct. Numerical experiments were carried out to ensure the independence of the results on the mesh, step sizes, and error tolerances. Use of a 31×31 cross-sectional grid, a 1.25×10^{-5} axial step size, and more stringent error tolerances had no significant effect on the solution.

Experimental Details

Experimental conversion data for formaldehyde and toluene were collected using the pilot-scale demonstration unit assembled in the United Technologies Research Center's (UTRC) laboratories. The configuration of this unit is well represented in Figure 1. The UTRC air-purification pilot unit is built into an 8 ft. (2.4 m) long, 1-ft $\times$ 1-ft^2 (0.3-m $\times$ 0.01-m^2) cross-section duct. The duct can accommodate up to five individual square monoliths and six lamp banks. Each of the six lamp banks can contain up to four UV lamps. Compressed fiberglass supported the monoliths and lamps, and formed the reactor wall. The duct's inner walls are coated with aluminum foil to reflect UV light. A blower at the reactor entrance provides the desired flow of unfiltered building air through the unit. Ultraviolet irradiation was provided by low-pressure mercury lamps (Voltrac G10T5L-S400), with 98% of the UV emitted at 254 nm. A UVC power meter (Oriel UVC Goldilux) was employed to measure UV intensity at the monolith faces.

The contaminants were generated either from a compressed-gas cylinder supply (toluene), or through a diffusion-controlled vaporizer (formaldehyde), and introduced at the inlet of the reactor. A Brüel & Kjaer 1302 multigas monitor was used to measure the concentrations of formaldehyde and water vapor. A gas chromatograph (IBM-9630) equipped with a 10% carbowax 20-M Chrom WAW 80–100-M packed column and flame ionization detector was used to measure toluene concentrations. Estimated absolute concentration uncertainties are ± 0.020 ppm$_v$ and ± 0.010 ppm$_v$ for formaldehyde and toluene, respectively.

Results and Discussion

The radiation field submodel reveals that the predicted dimensionless UV flux profile is uniquely determined by the TiO_2 thin-film reflectivity and the channel aspect ratio. For UV wavelength $\lambda = 254$ nm, the measured titania thin-film reflectivity ρ is equal to 0.055. Figure 3 shows the predicted UV photon wall-flux profile for a channel aspect ratio α equal to 8. The source-monolith spatial configuration causes a discontinuity in UV flux at the monolith mouth (the wall flux is only about half the incoming flux). This discontinuity at the channel mouth is a well-known characteristic of ballistic transport, and arises because of shadowing of the incoming diffuse light at the channel entrance by the wall. The UV flux drops sharply with increasing distance into the channel. At a reduced distance of one, the wall flux falls to less than 10% of the original incident flux value. At a reduced distance of only three, the wall flux falls to less than 1% of the incident flux; beyond this distance, the photocatalyst is essentially sub-

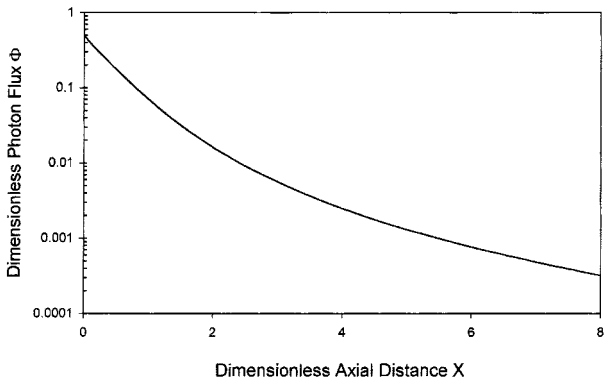

Figure 3. Predicted dimensionless wall intensity vs. dimensionless axial distance for square channels of aspect ratio α equal to 8 and reflectivity ρ equal to 0.055.

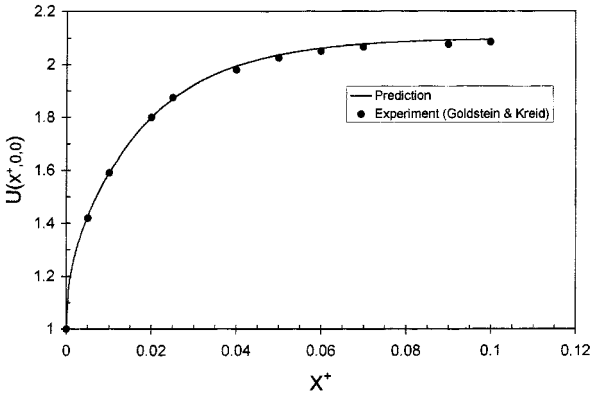

Figure 4. Axial velocity development at the duct center line.

Points are the experimental measurements of Goldstein and Kreid (1967); solid line is the model prediction.

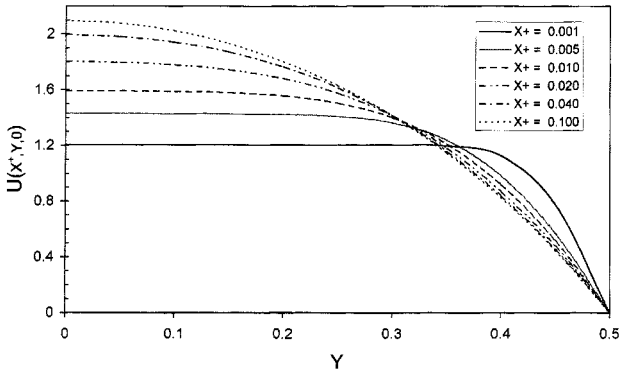

Figure 6. Axial velocity profile at the centerplane ($Z = 0$) as a function of dimensionless axial distance X^+.

ject to operation under dark conditions. Overall, the curve visually highlights the fact that only a limited part of the monolith can be effectively photoactivated. This inherent limitation should be considered in the design of honeycomb monolith PCO reactors.

Detailed results from the numerical solutions for the velocity field in a square duct are given now. To verify our numerical solutions, the predicted development of the center-line axial velocity is compared with the experiments of Goldstein and Kreid (1967) in Figure 4. Figure 5 compares the predicted axial pressure distribution with the measurements of Beavers et al. (1970). In both cases the numerical simulation results agree quite well with the experimental measurements. With confidence that our simulations yield accurate descriptions of the developing flow field, Figures 6–8 present model predictions of the axial and transverse velocity fields, and the concentration field for a representative set of conditions.

The development of axial velocity profiles $U(X^+, Y, 0)$ for different locations along the axial direction is presented in Figure 6. Near the entrance ($X^+ = 0.001$) the velocity profile is flat. As the fluid passes through the channel, the velocity profile becomes parabolic, until at about $X^+ = 0.10$, the flow is fully developed. Note that the difference between the velocity profile at $X^+ = 0.04$ and at $X^+ = 0.10$ is relatively modest.

Hydrodynamics of the fluid flow can be further understood by analyzing the transverse velocity in the cross section. Distribution of centerplane ($Z = 0$), Y-direction velocities (V) are shown in Figure 7. In the inlet region, flow resistance is larger near the channel walls, and hence fluid moves toward the hydrodynamic center. Away from the inlet region this difference in flow resistance becomes gradually smaller because of the higher axial velocity in the central region. This behavior explains why the transverse velocity is highest at the entrance region, and falls to essentially zero near the fully developed region. This transverse flow of fluid is responsible for the higher mass-transfer coefficients at the entrance region. Specifically, mass transfer toward the wall in the inlet region occurs by convection as well as diffusion, while mass transfer in the fully developed flow region occurs only by diffusion.

Figure 8 shows the centerplane ($Z = 0$) dimensionless formaldehyde concentration profile in the Y-direction at different axial positions for a fixed value of Re equal to 100 and a channel aspect ratio equal to 8. The concentration gradient is highest near the channel mouth, reflecting the higher VOC

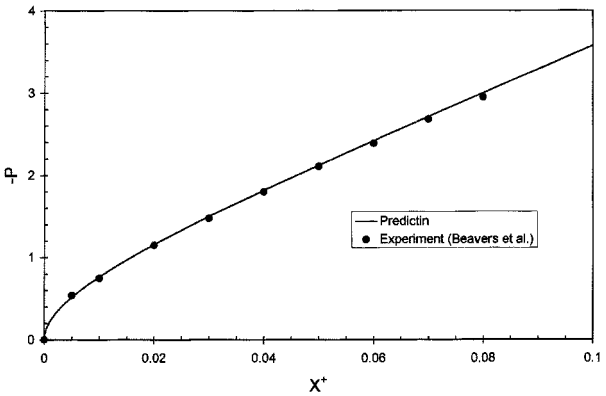

Figure 5. Axial pressure-drop profile.

Points are the experimental measurements of Beavers et al. (1970); solid line is the model prediction.

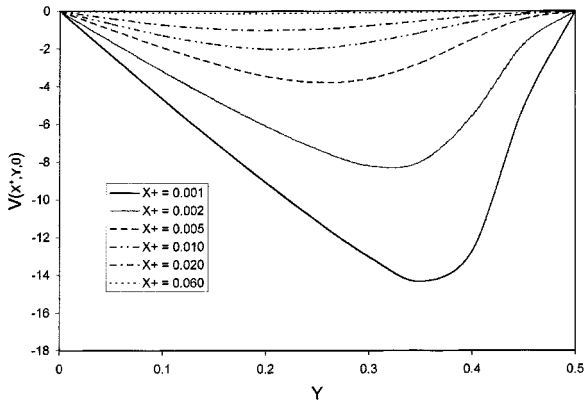

Figure 7. Transverse velocity distribution at the centerplane ($Z = 0$) as a function of dimensionless axial distance X^+.

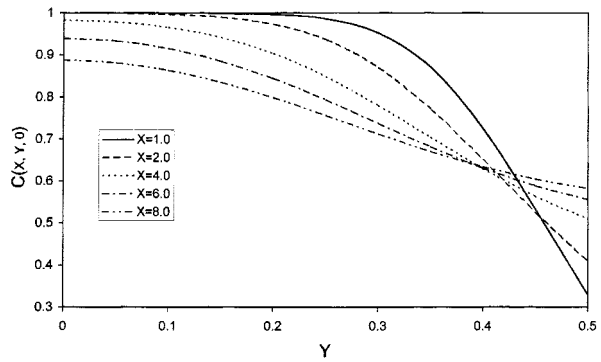

Figure 8. Concentration distribution of formaldehyde at the centerplane ($Z = 0$) for *Re* equal to 100, C_o equal to 2.1 ppm, C_w equal to 2,700 ppm, and I_o equal to 6.5 mW/cm^2 as a function of dimensionless axial distance *X*.

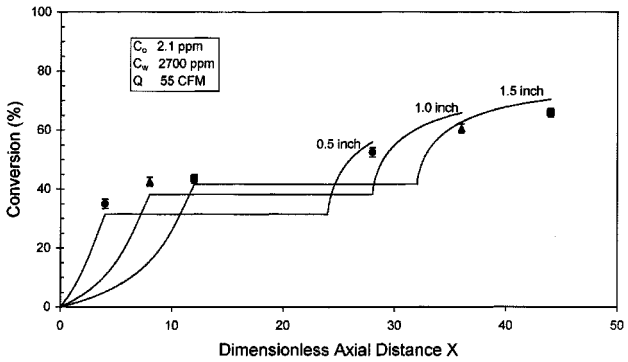

Figure 10. Model–experiment comparison for formaldehyde: effect of monolith channel length at fixed cell density.

destruction rates associated with high UV flux and high mass-transfer rate in this region. At a reduced distance *X* of one, the reactant concentration at the wall falls to approximately 32% of its inlet value. Gradually the concentration gradient becomes less severe as the UV flux driving the reaction dies away along the axial distance.

Figures 9 to 14 compare model predictions with the results of single-species (formaldehyde, toluene) conversion tests in the pilot-scale reactor. These experiments employed one to five honeycomb monoliths. Flow rates ranged from 55 to 410 cubic feed per min (CFM), with mean UV intensities on the $12'' \times 12''$ monolith faces of 6.0 to 6.5 mW/cm^2. Figure 9 shows a model–experiment comparison for formaldehyde conversion at an air flow rate of 55 CFM in a two-monolith/one-UV-lamp-bank configuration. Both monoliths contained 64 cells per square inch (CPSI) and were one inch in length, corresponding to a nominal channel aspect ratio α equal to 8. Conversion increases along the monolith length as photooxidation proceeds, and is unchanging in the void spaces between monoliths. Model predictions are, of course, independent of actual monolith spacing for a specified UV intensity; for clarity an arbitrary separation of 20 channel widths is shown for all model–experiment comparisons. The agreement between model and experiment is reasonable, given the difficulties of accurate air sampling and analysis at VOC concentrations in the 1–2 ppm$_v$ range and below.

The dependence of formaldehyde conversion on monolith length for otherwise fixed conditions of air flow rate, inlet formaldehyde concentration and water vapor concentration, and UV intensity are shown in Figure 10. The experimental tests employed a two monolith/single-UV-bank configuration. Monolith lengths were 0.5, 1.0 and 1.5 in. (12.7, 25.4, and 38.1 mm), corresponding to aspect ratios of 4, 8 and 12, respectively. The model predictions agree well with the experimental results. Both theory and experiment show that conversion increases modestly with increasing monolith length. This behavior reflects the modest penetration of UV light into the channels beyond four aspect ratios in length, as illustrated in Figure 3 for a monolith of aspect ratio equal to 8. For monoliths longer than about twelve aspect ratios in length, additional pressure drop will be incurred without realizing an enhancement in contaminant conversion.

The effect of total air flow rate on formaldehyde conversion for similar process conditions can be seen by comparing Figures 11 and 12. The modular nature of the duct-installed photocatalytic reactor allows accommodation of higher

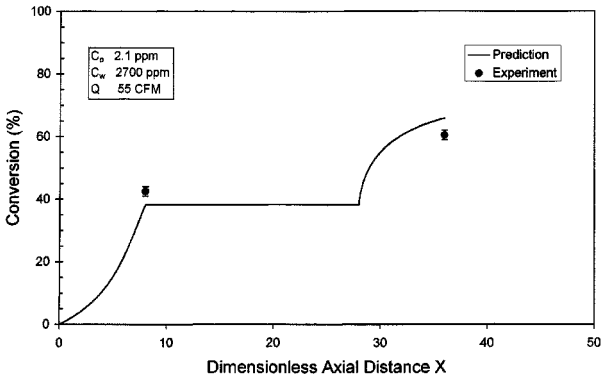

Figure 9. Model–experiment comparison for formaldehyde in a two-monolith/one-lamp-bank (2/1) configuration.

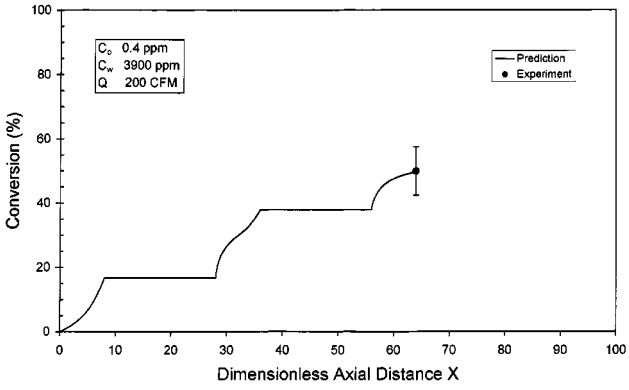

Figure 11. Model–experiment comparison for formaldehyde in a 3-monolith/2-lamp-bank configuration (3/2).

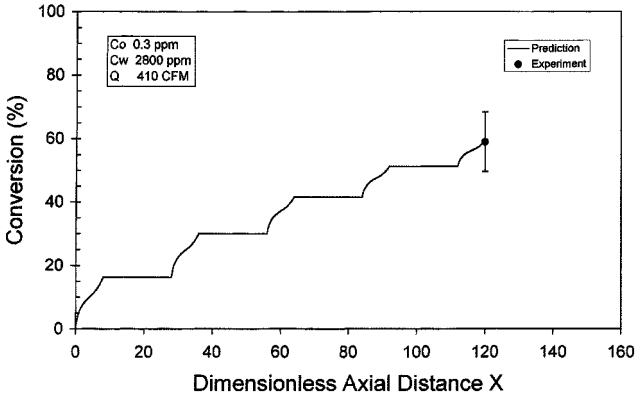

Figure 12. Model–experiment comparison for formaldehyde in a 5-monolith/6-lamp-bank configuration (5/6).

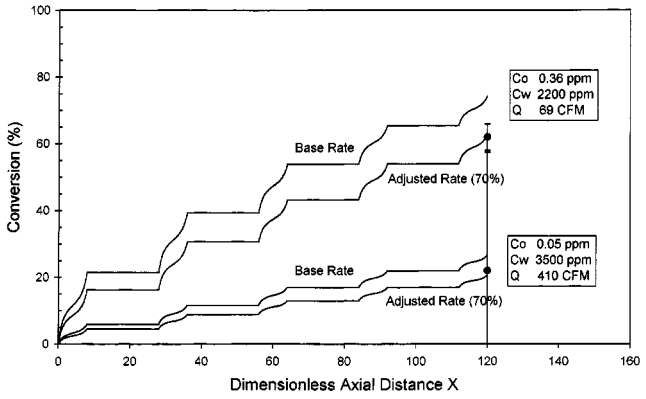

Figure 14. Theory–experiment comparison for toluene in a 5-monolith/6-lamp-bank configuration (5/6).

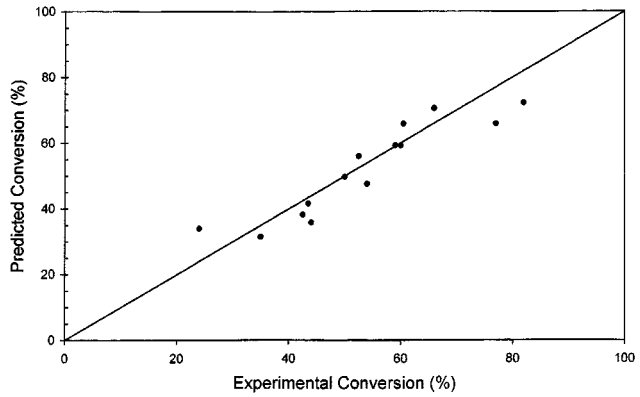

Figure 13. Overall theory–experiment comparison for formaldehyde.

throughput by incorporating additional UV lamp banks and monoliths. In this illustrative case, 200 ft^3/min (94 L/s) of air contaminated with 0.4 ppm_v formaldehyde is treated in a 3-monolith/2-lamp-bank configuration (Figure 11), while 410 ft^3/min (194 L/s) of air contaminated with 0.3 ppm_v formaldehyde is treated in a 5-monolith/6-lamp-bank configuration (Figure 12). In the former case, 50% conversion is achieved at the reactor outlet. In the latter case, 50% conversion is achieved at the outlet of the *fourth* monolith, with a conversion of nearly 60% realized at the duct outlet. In both cases, model predictions are in excellent agreement with experimental results.

Model-predicted and experimental results for all the formaldehyde conversion tests described previously, as well as some additional tests, are summarized in Table 1. Figure 13 shows the overall model–experiment comparison graphically. For a perfect match, all the data points should fall on the diagonal, which has a slope of one. A statistical best-fit line (not shown) through the points was found to have a slope of 0.96, with an R^2 of 0.825. This outcome indicates that the model is capable of predicting the experimental results with a high level of confidence. Remarkably, this excellent predictive capability was achieved *without benefit of any adjustable parameters.*

Figure 14 compares model predictions with experimental results for toluene conversion in a 5-monolith/6-lamp-bank

Table 1. Theory Experiment Comparison for Formaldehyde

Test	Flow Rate (ft^3/min)	UV Flux (mW/cm^2)	Inlet Conc. (ppm)	Water Conc. (ppm)	Lamp/ Surface	Monolith Length (in.)	Meas. Conv. (%)	Pred. Conv. (%)	Diff. (%)
1	200	6.5	0.40	3,900	8/4	1.0	50	49.75	0.5
2	200	6.5	0.40	3,900	16/8	1.0	82	72.27	11.87
3	410	6.5	0.30	2,800	8/4	1.0	24	34.01	−41.7
4	410	6.5	0.30	2,800	24/10	1.0	59	59.29	−0.49
5	55	6.5	1.9	6,000	4/1	1.0	44	35.87	18.47
6	55	6.5	1.9	6,000	4/2	1.0	77	65.87	14.45
7	55	6.5	2.1	2,700	4/1	0.5	35	31.52	9.94
8	55	6.5	2.1	2,700	4/2	0.5	52.5	56	−6.67
9	55	6.5	2.1	2,700	4/1	1.0	42.5	38.27	9.95
10	55	6.5	2.1	2,700	4/2	1.0	60.5	65.87	−8.87
11	55	6.5	2.1	2,700	4/1	1.5	43.5	41.69	4.16
12	55	6.5	2.1	2,700	4/2	1.5	66	70.49	−6.8
13	200	6.5	0.7	4,800	8/4	1.0	54	47.63	11.8
14	410	6.5	0.3	2,800	24/10	1.0	60	59.26	1.23

SI conversion: L/s = ft^3/min × 0.472; mm = in. × 25.4.

Table 2. Theory Experiment Comparison for Toluene

Test	Flow Rate (ft^3/min)	UV Flux (mW/cm^2)	Inlet Conc. (ppm)	Water Conc. (ppm)	Lamp/ Surface	Monolith Length (in.)	Meas. Conv. (%)	Pred. Conv. (%)	Diff. (%)
1	63	6.5	0.30	3,500	24/10	1.0	68	70.11	−3.10
2	210	6.5	0.10	3,500	24/10	1.0	38	34.23	9.92
3	410	6.5	0.05	3,500	24/10	1.0	22	20.69	5.95
4	210	6.5	0.30	3,800	24/10	1.0	26	29.58	−13.77
5	63	6.5	0.30	5,800	24/10	1.0	62	68.23	−10.05
6	69	6.5	0.36	2,200	24/10	1.0	62	63.06	−1.70

SI conversion: $L/s = ft^3/min \times 0.472$; mm = in. × 25.4.

configuration. Two cases are included, one with air contaminated with 0.36 ppm_v toluene at a flow rate of 69 ft^3/min (33 L/s), and the second with air contaminated with 0.05 ppm_v toluene at a flow rate of 410 ft^3/min (194 L/s). The significantly higher conversion in the former case reflects both the higher contact time at the lower flow rate, and the lesser inhibition by water vapor associated with the lower humidity level in the air. In both cases the model tends to overpredict the experimental toluene conversions. To obtain better model–experiment agreement the intrinsic reaction rate constant (K_o) was adjusted to 70% of the literature value. In all other model–experiment comparisons for toluene, this 70% adjustment factor was used. Table 2 and Figure 15 summarize the overall model–experiment comparison for toluene. Figure 15 reveals that the model with the single adjustable kinetic parameter matches the data quite well.

The fact that a reaction-rate parameter for toluene required empirical adjustment, while the formaldehyde rate parameters yielded accurate simulations without adjustment suggests that the toluene data are influenced by a systematic inaccuracy. It is well known that aromatic compounds (such as Ameen and Raupp, 1999; Jacoby et al., 1996), and toluene in particular (Luo and Ollis, 1996), are capable of reversibly deactivating titania during photocatalytic oxidation. Partial catalyst deactivation could account for the discrepancy between the toluene conversion measurements and the model predictions. Alternatively, conversion behavior of a single contaminant may be influenced by the presence of a second contaminant through competitive adsorption effects or the creation of additional reaction pathways (Sauer et al., 1995). We conclude that a second possible explanation for the systematic model–experiment mismatch with toluene is that the unfiltered laboratory-building air employed in the pilot-scale toluene conversion experiments was contaminated by one or more unquantified gaseous contaminants. In any case, the lack of perfect agreement between the model predictions and the experimental conversions should not be viewed as a model failure, since a rule of thumb for kinetics experiments holds that kinetic parameters can generally be determined only to within a factor of 2. The adjustment factor employed for toluene falls well within this accuracy limit. Indeed, the demonstrated predictive capability of the reactor model suggests that the monolith configuration would serve as an excellent vehicle for conducting kinetics experiments.

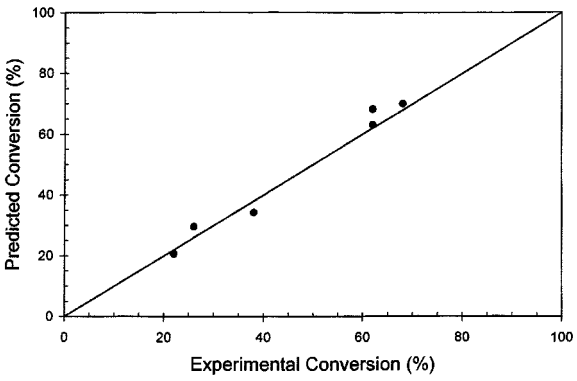

Figure 15. Overall theory–experiment comparison for toluene.

Model predictions for a third single-contaminant data set, specifically, for *n*-hexane, consistently overpredict the experimental conversion measurements. Because *n*-hexane is only weakly adsorbed on titania, it seems likely that the presence of unknown, more strongly bound cocontaminants inhibited the photocatalytic oxidation of *n*-hexane in the pilot-scale unit, leading to substantially lower conversion than expected (Bendfeldt et al., 1998). This hypothesis could be readily tested by conducting controlled cocontaminant conversion studies in bench-scale monolith reactors.

The present three-dimensional model predictions are in general somewhat more accurate (although not dramatically so) than those of the one-dimensional model developed by Hall (1996) at UTRC. For example, the one-dimensional model consistently overpredicts pilot-scale performance data; to obtain a good experiment–model match, an empirical adjustment factor on the formaldehyde photocatalytic destruction rate of 0.75 was employed. The observed modest improvement in model-predictive capability might be attributed to the approximation inherent in the one-dimensional model created by *averaging* the mass-transfer coefficients over the channel length, although we have not verified this hypothesis by performing one-dimensional model calculations employing *local* mass-transfer coefficients. Given the significantly greater computational effort for the three-dimensional model, this work confirms the value of the one-dimensional model for commercial design purposes. On a more fundamental note, a study employing experimental conversion measurements and direct comparison of the predictions of both models may provide a unique vehicle for the investigation and quantification of mass-transfer coefficients.

Conclusions

A single-channel convection–diffusion–reaction model accounting rigorously for developing fluid flow in the entrance

length and the UV axial flux profile provides an accurate description of single-contaminant conversion in a pilot-scale monolith-based air-purification unit. This rigorous first-principles mathematical model provides a sound theoretical basis for quantifying the inherent UV energy utilization capabilities and performance limitations of a honeycomb monolith photocatalytic reactor for air purification. Once fully validated, the model could be used in photocatalytic reactor design, optimization and control, and to develop quantitative energy utilization metrics for use by IAQ and HVAC engineers.

Acknowledgments

The ASU authors gratefully acknowledge the financial support of the U.S. Environmental Protection Agency for partial support of this work. We also thank Dr. Robert J. Hall of UTRC for his critical review of the manuscript and valuable suggestions for its improvement.

Literature Cited

Ameen, M. M., and G. B. Raupp, "Reversible Catalyst Deactivation During *o*-Xylene Photocatalytic Oxidation," *J. Catal.* (1999).

Beavers, G. S., E. M. Sparrow, and R. A. Magnuson, "Experiments on Hydrodynamically Developing Flow in Rectangular Ducts of Arbitrary Aspect Ratio," *Int. J. Heat Mass Transfer*, **33**, 689 (1970).

Bendfeldt, P., R. J. Hall, T. N. Obee, S. O. Hay, and J. J. Sangiovanni, "A Feasibility Study of Photocatalytic Air Purification for Commercial Passenger Airliners," United Technologies Research Center Rep. R97-1.300.9702 (1997).

Bendfeldt, P., R. J. Hall, T. N. Obee, S. O. Hay, and J. J. Sangiovanni, "Computational and Experimental Studies of UV/Titania Photocatalytic Oxidation of VOCs in Honeycomb Monoliths," *J. Adv. Oxid. Technol.* (1998).

Brucato, A., F. Grisafi, and R. Urso, "Economic Evaluation of Photon Sources for Photocatalytic Applications by Means of Spectral Distribution Analysis," *Int. Conf. on TiO_2 Photocatalytic Treatment of Water and Air*, Orlando, FL, p. 48 (1997).

Carnahan, B., H. Luther, and J. O. Wilkes, *Applied Numerical Methods*, Wiley, New York (1969).

Chou, F. C., and G. J. Hwang, "Vorticity-Velocity Method for the Graetz Problem and the Effect of Natural Convection in a Horizontal Rectangular Channel with Uniform Wall Heat Flux," *J. Heat Transfer*, **109**, 704 (1987).

Dibble, L. A., and G. B. Raupp, "Kinetics of the Gas-Solid Heterogeneous Photocatalytic Oxidation of Trichloroethylene by Near-UV Illuminated Titanium Dioxide," *Catal. Lett.*, **4**, 345 (1990).

Dibble, L. A., and G. B. Raupp, "Fluidized Bed Photocatalytic Oxidation of Trichloroethylene in Contaminated Air Streams," *Environ. Sci. Technol.*, **26**, 492 (1992).

Fu, X., W. A. Zeltner, and M. A. Anderson, "The Gas-Phase Photocatalytic Mineralization of Benzene on Porous Titania-Based Catalyst," *Appl. Catal. B*, **6**, 209 (1995).

Goldstein, R. J., and D. K. Kreid, "Measurement of Laminar Flow Development in a Square Duct Using a Laser-Doppler Flowmeter," *J. Appl. Mech.*, **89**, 813 (1967).

Groppi, G., A. Belloli, E. Tronconi, and P. Forzatti, "Analysis of Multidimensional Models of Monolith Catalyst for Hybrid Combustor," *AIChE J.*, **41**, 2250 (1995a).

Groppi, G., A. Belloli, E. Tronconi, and P. Forzatti, "A Comparison of Lumped and Distributed Models of Monolith Catalytic Combustors," *Chem. Eng. Sci.*, **50**, 2705 (1995b).

Hall, R. J., T. N. Obee, S. O. Hay, J. J. Sangiovanni, P. A. Boncyk, J. D. Freihaut, J. E. Genovese, and F. Sribnik, "Photocatalytic Oxidation Technology for Trace Contaminant Control in Aircraft and Spacecraft," SAE Paper 961520, SAE, Warrendate, PA (1996).

Hay, S. O., T. N. Obee, J. D. Freihaut, and R. W. Marsh, "Photocatalytic Bioaerosol Control," *2nd Int. Conf. on TiO_2 Photocatalytic Treatment of Water and Air Abstracts*, Cincinnati, OH, p. 33 (1996).

Hayes, R. E., S. T. Kolaczkowski, and W. J. Thomas, "Finite Element Model for a Catalytic Monolith Reactor," *Comput. Chem. Eng.*, **16**, 645 (1992).

Hayes, R. E., S. T. Kolaczkowski, W. J. Thomas, and J. Titiloye, "Transient Experiments and Modeling of the Catalytic Combustion of Methane in a Monolith Reactor," *Ind. Eng. Chem. Res.*, **35**, 406 (1996).

Hossain, Md. M., and G. B. Raupp, "Radiation Field Modeling in a Photocatalytic Monolith Reactor," *Chem. Eng. Sci.*, **53**, 3771 (1998a).

Hossain, Md. M., and G. B. Raupp, "Modeling of a Photocatalytic Honeycombed Monolith Reactor for Air Purification Processes," *J. Adv. Oxid. Technol.*, **3**, 285 (1998b).

Hossain, Md. M., and G. B. Raupp, "Polychromatic Radiation Field Model for a Honeycomb Monolith Photocatalytic Reactor," *Chem. Eng. Sci.*, in press (1999).

Howang, G. J., Y. C. Cheng, and M. L. Ng, "Developing Laminar Flow and Heat Transfer in a Square Duct with One-Walled Injection and Suction," *Int. J. Heat Mass Transfer*, **36**, 2429 (1993).

Jacoby, W. A., D. M. Blake, J. A. Fennell, J. E. Boulter, L. M. Vargo, M. C. George, and S. K. Dolberg, "Heterogeneous Photocatalysis for Control of Volatile Organic Compounds in Indoor Air," *J. A&WMA*, **46**, 891 (1996).

Kikuchi, Y., K. Sunada, T. Iyoda, K. Hashimoto, and A. Fujishima, "Photocatalytic Bactericidal Effect of TiO_2 Thin Films: Dynamic View of the Active Oxygen Species Responsible for this Effect," *J. Photochem. Photobiol. A: Chem.*, **106**, 51 (1997).

Luo, Y., "Reactor Analysis for Heterogeneous Photocatalytic Air Purification Processes," PhD Diss., North Carolina State University, Raleigh (1994).

Luo, Y., and D. F. Ollis, "Heterogeneous Photocatalytic Oxidation of Trichloroethylene and Toluene Mixtures in Air: Kinetic Promotion and Inhibition, Time-Dependent Catalyst Activity," *J. Catal.*, **163**, 1 (1996).

National Research Council, *Potential Applications of Concentrated Solar Photons*, Academy Press, Washington, DC (1991).

Nicolella, C., and M. Rovatti, "Mathematical Modeling of Monolith Reactors for Photocatalytic Oxidation of Air Contaminants," *Chem. Eng. J.*, **69**, 119 (1998).

Nimlos, M. R., E. J. Wolfrum, M. L. Brewer, J. A. Fennel, and G. Bintner, "Gas-Phase Heterogeneous Photocatalytic Oxidation of Ethanol: Pathways and Kinetic Modeling," *Environ. Sci. Technol.*, **30**, 3102 (1996).

Obee, T. N., "Photooxidation of Sub-Parts-per-Million Toluene and Formaldehyde Levels on Titania Using a Glass-Plate Reactor," *Environ. Sci. Technol.*, **30**, 3578 (1996).

Obee, T. N., and R. B. Brown, "TiO_2 Photocatalysis for Indoor Air Applications: Effects of Humidity and Trace Contaminant Levels on the Oxidation Rates of Formaldehyde, Toluene, and 1,3-Butadiene," *Environ. Sci. Technol.*, **29**, 1223 (1995).

Peral, J., and D. F. Ollis, "Heterogeneous Photocatalytic Oxidation of Gas-Phase Organics for Air Purification: Acetone, 1-Butanol, Butyraldehyde, Formaldehyde, and *m*-Xylene Oxidation," *J. Catal.*, **136**, 554 (1992).

Raupp, G. B., and C. T. Junio, "Photocatalytic Oxidation of Oxygenated Air Toxics," *Appl. Surf. Sci.*, **72**, 321 (1993).

Roache, P. J., *Computational Fluid Dynamics*, Reinhold, New York, p. 61 (1971).

Sauer, M. L., and D. F. Ollis, "Acetone Oxidation in a Photocatalytic Monolith Reactor," *J. Catal.*, **149**, 81 (1994).

Sauer, M. L., M. A. Hale, and D. F. Ollis, "Heterogeneous Photocatalytic Oxidation of Dilute Toluene-Chlorocarbon Mixtures in Air," *J. Photochem. Photobiol. A: Chem.*, **88**, 169 (1995).

Siegel, R., and J. R. Howell, *Thermal Radiation Heat Transfer*, 3rd ed., McGraw-Hill, New York (1992).

Sunada, K., Y. Kikuchi, K. Hashimoto, and A. Fujishima, "Bactericidal and Detoxification Effects on TiO_2 Thin Film Photocatalysts," *Environ. Sci. Technol.*, **32**, 726 (1998).

"Total Exposure Assessment Methodology (TEAM) Study," Rep. 600/6-87/002a, U.S. EPA, Washington, DC (1987).

Vortuba, J., J. Sinkule, V. Hlavacek, and J. Skrivanek, "Heat and Mass Transfer in Honeycomb Catalysts—I," *Chem. Eng. Sci.*, **30**, 117 (1975a).

Vortuba, J., O. Mikus, K. Nguen, V. Hlavacek, and J. Skrivanek,

''Heat and Mass Transfer in Honeycomb Catalysts: II,'' *Chem. Eng. Sci.*, **30**, 201 (1975b).
Vrentas, J. S., J. L. Duda, and K. G. Bargeron, ''Effect of Axial Diffusion of Vorticity on Flow Development in Circular Conduits: I. Numerical Simulations,'' *AIChE J.*, **12**, 837 (1966).
Worth, D. J., A. Spence, and P. I. Crumpton, ''Radiative Exchange Between Square Parallel Channels in a Concentric Monolith Structure,'' *Int. J. Heat Mass Transfer*, **39**, 1463 (1996).
Young, L. C., and B. A. Finlayson, ''Mathematical Models of the Monolith Catalytic Converter: 1. Development of Model and Application of Orthogonal Collocation,'' *AIChE J.*, **22**, 331 (1976).

Manuscript received Nov. 19, 1998, and revision received Mar. 15, 1999.